

PERSPECTIVE

In-plane anisotropic two-dimensional materials for twistronics

To cite this article: Hangyel Kim et al 2024 Nanotechnology 35 262501

View the article online for updates and enhancements.

You may also like

- Twisted charge-density-wave patterns in bilayer 2D crystals and modulated electronic states
- Yaoyao Chen, Liwei Liu, Xuan Song et al.
- Highly in-plane anisotropic 2D semiconductors -AuSe with multiple superior properties: a first-principles investigation

Peng-Lai Gong, Fang Zhang, Liang Li et

- <u>Atomic frustration-based twistronics</u>
W N Mizobata, J E Sanches, M Penha et



Perspective

In-plane anisotropic two-dimensional materials for twistronics

Hangyel Kim^{1,11}, Changheon Kim^{1,2,11}, Yeonwoong Jung^{3,4,5}, Namwon Kim^{6,7,8}, Jangyup Son^{2,9,10}, and Gwan-Hyoung Lee^{1,6}

¹ Department of Material Science and Engineering, Seoul National University, Seoul 08826, Republic of Korea ² Functional Composite Materials Research Center, Korea Institute of Science and Technology (KIST), Jeonbuk 55324, Republic of Korea ³ NanoScience Technology Center, University of Central Florida, Orlando, FL 32826, United States of America

- ⁴ Department of Materials Science and Engineering, University of Central Florida, Orlando, FL 32816, United States of America
- ⁵ Department of Electrical and Computer Engineering, University of Central Florida, Orlando, FL 32816, United States of America
- ⁶ Research Institute for Advanced Materials (RIAM), Seoul National University, Seoul 08826, Republic of Korea
- ⁷ Ingram School of Engineering, Texas State University, San Marcos, TX 78666, United States of America ⁸ Materials Science, Engineering, and Commercialization, Texas State University, San Marcos, TX 78666, United States of America ⁹ Department of JBNU-KIST Industry-Academia Convergence Research, Jeonbuk National University, Jeonbuk 54895, Republic of Korea ¹⁰ Division of Nano and Information
- Technology, KIST School University of Science and Technology(UST), Jeonbuk 55324, Republic of Korea E-mail: gwanlee@snu.ac.kr Published 12 April 2024

Abstract

In-plane anisotropic two-dimensional (2D) materials exhibit in-plane orientation-dependent properties. The anisotropic unit cell causes these materials to show lower symmetry but more diverse physical properties than in-plane isotropic 2D materials. In addition, the artificial stacking of in-plane anisotropic 2D materials can generate new phenomena that cannot be achieved in in-plane isotropic 2D materials. In this perspective we provide an overview of representative in-plane anisotropic 2D materials and their properties, such as black phosphorus, group IV monochalcogenides, group VI transition metal dichalcogenides with 1T' and T_d phases, and rhenium dichalcogenides. In addition, we discuss recent theoretical and experimental investigations of twistronics using in-plane anisotropic 2D materials. Both in-plane anisotropic 2D materials and their twistronics hold considerable potential for advancing the field of 2D materials, particularly in the context of orientation-dependent optoelectronic devices.

Keywords: two-dimensional materials, in-plane anisotropy, van der Waals heterostructure, moiré superlattice, twistronics

1. Introduction

Two-dimensional (2D) materials consist of layers that are weakly stacked together through van der Waals (vdW) forces, whereas the atoms in each layer are strongly bound to each other by covalent or ionic bonds. This difference in bonding creates an anisotropy between the in-plane and out-of-plane directions, which also enables the exfoliation and isolation of a single layer of material [1] and advancing investigations on exotic phenomena, such as the quantum Hall effect in graphene [2–4], the strongly bound excitons and trions in group VI transition metal dichalcogenides (TMDCs) [5, 6], the development of hexagonal boron nitride (hBN) as a 2D dielectric material [7, 8], and the fabrication of vdW heterostructures and their optoelectronic devices [9–11]. These 2D materials exhibit high symmetry within their in-plane structures, resulting in nearly isotropic in-plane properties.

In contrast, there are several groups of 2D materials with in-plane anisotropy, referred to as in-plane anisotropic 2D materials. Because of the different lattice constants and bonding configurations within their in-plane orientations, they exhibit highly anisotropic mechanical, electrical, and optical properties. This category includes black phosphorus, which is the most representative in-plane anisotropic 2D material, group IV monochalcogenides, 1T' or T_d phase MoTe₂ and WTe₂, and rhenium dichalcogenides. As the presence of anisotropy between the in-plane and out-of-plane directions has prompted and widened research on 2D materials, the high degree of freedom of in-plane anisotropic 2D materials also has potential to provide and unlock new opportunities and possibilities of these materials.

The investigation of in-plane anisotropic 2D materials follows the approach employed for in-plane isotropic 2D materials, which involves the artificial stacking of these materials with lattice mismatch or relative twist angles. The

¹¹ These authors contributed equally to this work

incommensurate stacking of 2D materials generates quasiperiodic geometric patterns denoted to as moiré superlattices [12–14]. These patterns can modulate the electronic properties of 2D materials and generate non-trivial physical phenomena that are absent in their individual layers. This approach is referred to as twistronics; the properties and phenomena induced by twistronics have been widely studied in in-plane isotropic 2D materials, such as superconductivity and Mott-like insulating states in twisted bilayer graphene [15, 16], out-of-plane ferroelectricity in artificially stacked hBN and TMDCs [17–20], and moiré interlayer excitions in twisted bilayers of TMDCs [21–23]. The artificial stacking of in-plane anisotropic 2D materials is expected to lead to a broader range of unique phenomena owing to their higher degrees of freedom. Research on this topic is gradually emerging, showing promise for future exploration.

From this perspective, we present a comprehensive overview of in-plane anisotropic 2D materials and their twistronics. Initially, we introduce representative examples of in-plane anisotropic 2D materials and their respective characteristics based on their crystal structures. In the subsequent section, we review the recent progress in twistronics composed of in-plane anisotropic 2D materials, encompassing both vdW homobilayers and heterostructures. Lastly, we address several challenges and prospects associated with these emerging materials.

2. In-plane anisotropic 2D materials

Orientation-dependent properties of in-plane anisotropic 2D materials are mainly attributed to their low crystallographic symmetry. Unlike in-plane isotropic 2D materials with hexagonal or trigonal symmetry, such as graphene, group VI TMDCs, and hBN, most in-plane anisotropic 2D materials exhibit orthorhombic, monoclinic, or triclinic crystal systems. These crystal systems show nonequivalent lattice parameters and bonding configurations that depend on the in-plane orientations of the material. Consequently, the physical properties of in-plane anisotropic 2D materials, including their mechanical, electrical, optical, and thermal properties, show a distinctive dependence on the in-plane orientation. In table 1, we categorise in-plane anisotropic 2D materials based on their crystal systems and summarise their space groups, band structures, electrical anisotropy ratios, and remarkable characteristics. The electrical anisotropy ratio refers the ratio between electrical properties (resistance (R), conductance (G), or mobility (μ)) along each principle in-plane crystallographic axis.

2.1. Black phosphorus: representative in-plane anisotropic 2D materials

Black phosphorus (BP), which is also known as phosphorene, is the most extensively investigated in-plane anisotropic 2D material. The crystal structure of BP is shown in figure 1(a). BP has an orthorhombic structure with the Cmca space group. The monolayer of BP is characterised by a puckered arrangement composed of two subatomic layers, which arise from the repulsion between the lone pair electrons in the phosphorus atoms. As confirmed in the top-view image (right side of figure 1(a)), BP exhibits distinct lattice constants and bonding configurations along the armchair (x) and zigzag (y) directions. These differences give rise to in-plane anisotropic properties.

Firstly, BP exhibits highly anisotropic in-plane mechanical properties. Theoretical calculations have shown that the Young's modulus of monolayer BP along the armchair direction ($E_{\rm armchair}$) is smaller than that along the zigzag direction ($E_{\rm zigzag}$) [24, 25]. This difference results from the puckered structure of BP along the armchair direction. Under compression or tension, the pucker can be compressed or flattened rather than extending the bonding length between the P atoms. This behaviour facilitates mechanical deformation along the armchair

Crystal system	Materials	Space group (mono/bulk)	Band gap (eV) (mono/bulk)	Band structure (mono/bulk)	Electrical anisotropy ratio	Remarkable characteristics
Orthorhombic	ВР	Pnma / Cmca	1.6/0.68 [27]	Direct/Direct [27]	G ratio ~ 1.5 [32]	Direct band gap from mono to bulk
	MX (M: Ge, Sn/X: S, Se)	Pnm2 ₁ / Pnma	SnS: 2.24/ [50] SnSe: 1.39/ [50] GeS: 2.74/ [50] GeSe: 1.66/ [50]	SnS: Indirect/Indirect [50] SnSe: Indirect/Indirect [50] GeS: Indirect/Indirect [50] GeSe: Direct/Indirect [50]	GeS: μ ratio \sim 4.1 [119] GeSe: μ ratio \sim 1.85 [120]	In-plane ferroelectricity
	T_d -MoTe ₂ , WTe ₂	$P2_1/m / Pnm2_1$	Semi-metal	,		Topologically non-trivial
Monoclinic	1T'-MoTe ₂ , WTe ₂	$P2_1/m / P2_1/m$	Semi-metal		WTe ₂ : R ratio ~ 3 [76]	
Triclinic	ReS ₂ , ReSe ₂	PĪ/ PĪ	ReS ₂ : 1.6/1.5 [85] ReSe ₂ : 1.31/1.06 [121]	ReS ₂ : Direct/Indirect [90] ReSe ₂ : Indirect/Indirect [121]	ReS ₂ : μ ratio ~3.1 [79]	Ferroelasticity

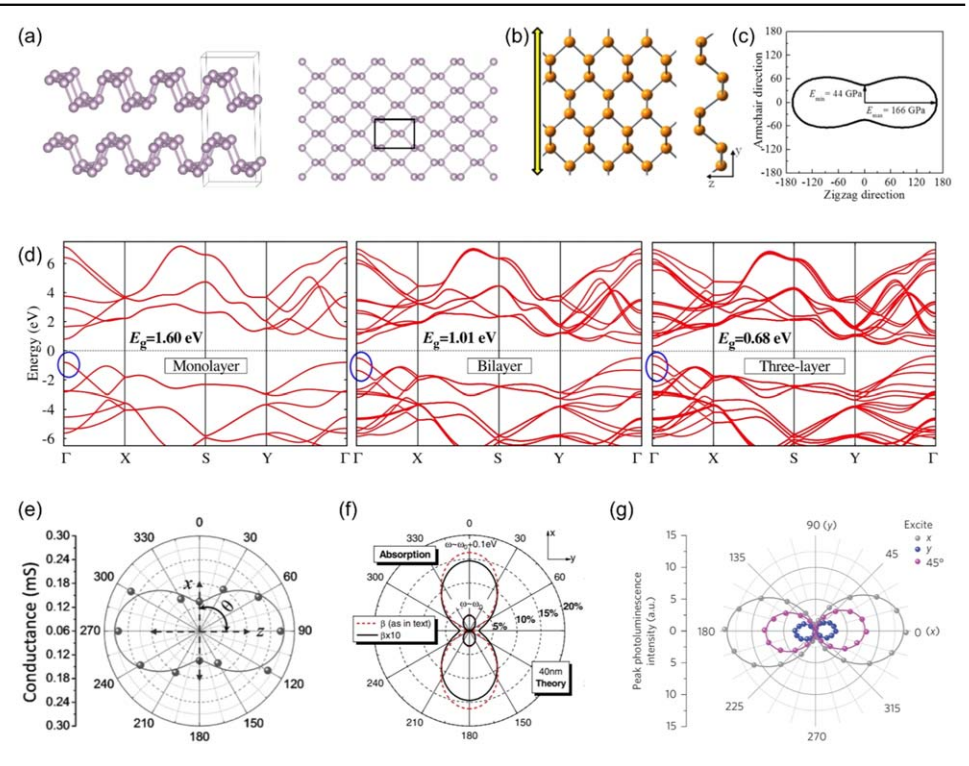


Figure 1. Black phosphorus. (a) Crystal structure of BP viewed from side (left) and top (right). Unit cells are represented with black solid lines. (b), (c) mechanical anisotropy of BP. (b) Flattening of pucker in BP under tensile strain along the armchair direction. (c) Polar plot of calculated in-plane Young's modulus. (b), (c) were adapted from [24] with permission. (d) Calculated band structures of mono-, bi-, and trilayer BP. Adapted from [28] with permission. (e)–(g) Polar plots of experimental polar plots of (e) DC conductance, (f) calculated absorption coefficient as a function of light polarization angle, (g) photoluminescence peak intensity as a function of analyzer angle for excitation along armchair, zigzag, and 45° directions. Adapted from [33, 37, 38] respectively, with permission.

direction (figure 1(b)) [24, 25]. The polar plot in figure 1(c) shows the in-plane Young's modulus of monolayer BP obtained from the density functional theory (DFT) [24]. The Young's modulus along the zigzag direction ($E_{\rm zigzag} = 166$ GPa) is approximately four times larger than that along the armchair direction ($E_{\rm armchair} = 44$ GPa). Similarly, the critical strain along the armchair direction (30%) is slightly larger than that along the zigzag direction (27%) [24]. Several experimental studies have investigated the mechanical properties of BP. Notably, measurements of $E_{\rm armchair}$ and $E_{\rm zigzag}$ of few-layer BP using nanoindentation and buckling metrology show that the zigzag direction is stiffer than the armchair direction [26, 27], which are consistent with theoretical calculations [24, 25].

BP also exhibits anisotropic in-plane electrical properties. Figure 1(d) shows the electronic band structure of monolayer, bilayer, and trilayer BP [28]. Regardless of its thickness, BP shows a direct band gap, which gradually decreases from 1.6 to 0.68 eV when transitioning from a monolayer to a trilayer structure. In addition, the band structure also indicates that the curvature along the Γ -X (armchair) direction is smaller than that along the Γ -Y (zigzag) direction for both the conduction band minimum (CBM) and valence band maximum (VBM) [28–32]. These differences suggest that both for electrons and holes, the effective mass along the armchair direction is smaller than that along zigzag direction. Qiao *et al* theoretically investigated the effective mass of charge carriers in BP from the monolayer to the bulk [30]. In the case of the monolayer, the effective mass of electrons along the armchair and zigzag directions is $0.17m_0$ and $1.12m_0$, and that of holes is $0.15m_0$ and $6.35m_0$, respectively, where m_0 is the rest electron mass. As the carrier mobility is inversely proportional to the effective mass, BP exhibits

anisotropic carrier mobility and direct current (DC) conductance within its plane (figure 1(e)) [33–35]. However, it should be noted that the effective mass is not the only factor that influences the anisotropy ratio of carrier mobility, as mobility is also affected by other factors, such as scattering by phonons and charged impurities [30, 36].

The anisotropic band dispersion of BP also results in anisotropic in-plane optical properties. BP has a mirror plane perpendicular to the armchair direction, and the electron wavefunctions at the CBM and VBM include s, p_x , and p_z orbitals with even symmetry with respect to the mirror plane. As linearly polarized light along y-axis exhibits an odd symmetry with respect to the mirror plane, the absorption of y-polarized light is forbidden [30–32]. Hence, BP exhibits higher absorption in the Γ -X direction (lower in the Γ -Y) when the polarization of the incident light is parallel to the respective direction (figure 1(f)) [31, 32, 37]. Furthermore, the photoluminescence (PL) of BP displayed in-plane anisotropy (figure 1(g)) [31, 38]. As previously mentioned, charge carriers exhibit higher mobility along the armchair direction due to the smaller effective mass along that direction. Conversely, the Coulomb interaction remains isotropic regardless of the direction. As a result, anisotropic excitons are generated, leading to strong polarization of the PL along the armchair direction.

In addition to the aforementioned properties, other physical properties exhibit distinctive in-plane anisotropies, such as reflection [39, 40], thermal transport [41, 42], and Raman scattering [43, 44].

Despite its outstanding properties, the applications of BP have been limited because of its instability in the presence of oxygen and water, which can react with its lone pair electrons [45, 46]. To ensure a meticulous investigation, the exfoliation, characterisation, and manipulation of BP are recommended to be performed under inert conditions. Encapsulation with materials such as AlO_x [47], hBN [48], and native oxides [49] is another possible solution for preventing the degradation of BP.

2.2. Group IV monochalcogenides: in-plane ferroelectricity

Group IV monochalcogenides (MX, M = Ge or Sn, X = S or Se) have crystal structures similar to those of BP. Unlike the single-element composition of BP, MXs are binary systems comprising two elements with different electronegativities. Furthermore, in contrast to BP, which has two atomic sublayers, MXs' atomic layers consist of four sublayers (figure 2(a)). Hence, the MXs exhibit lower symmetry compared to BP within the Pnma space group. In particular, the monolayers exhibit a broken inversion symmetry.

Theoretical results by Xu *et al* indicate that monolayer SnS, SnSe, GeS, and GeSe have bandgaps of 2.24, 1.39, 2.74, and 1.66 eV, respectively. Notably, GeSe is predicted to possess a direct band gap (figure 2(b)) [50].

By combination of the electronegativity difference between the metal and chalcogen atoms and noncentrosymmetry in their monolayer, odd-layered MXs show in-plane ferroelectricity along the armchair direction (red arrows in figure 2(a)) [51–56]. In contrast, even-layered MXs exhibit antiferroelectric characteristics, because the opposite polarizations are cancelled out by the adjacent layers. Nevertheless, depending on the stacking order, the even-layered MXs can exhibit ferroelectricity. Sutter *et al* confirmed stacking order-dependent in-plane ferroelectricity in SnS using lateral piezoresponse force microscopy (PFM) as shown in figure 2(c) [55]. The upper (lower) panels of figure 2(c) correspond to the topography, PFM amplitude, and PFM phase images of AB-stacked (AA-stacked) SnS. The alternating (increasing) lateral PFM amplitude and phase images indicate the annihilation (accumulation) of in-plane ferroelectricity in AB-stacked (AA-stacked) SnS. This result is supported by the cross-sectional transmission electron microscopy (TEM) images obtained by Higashitarumizu *et al*,

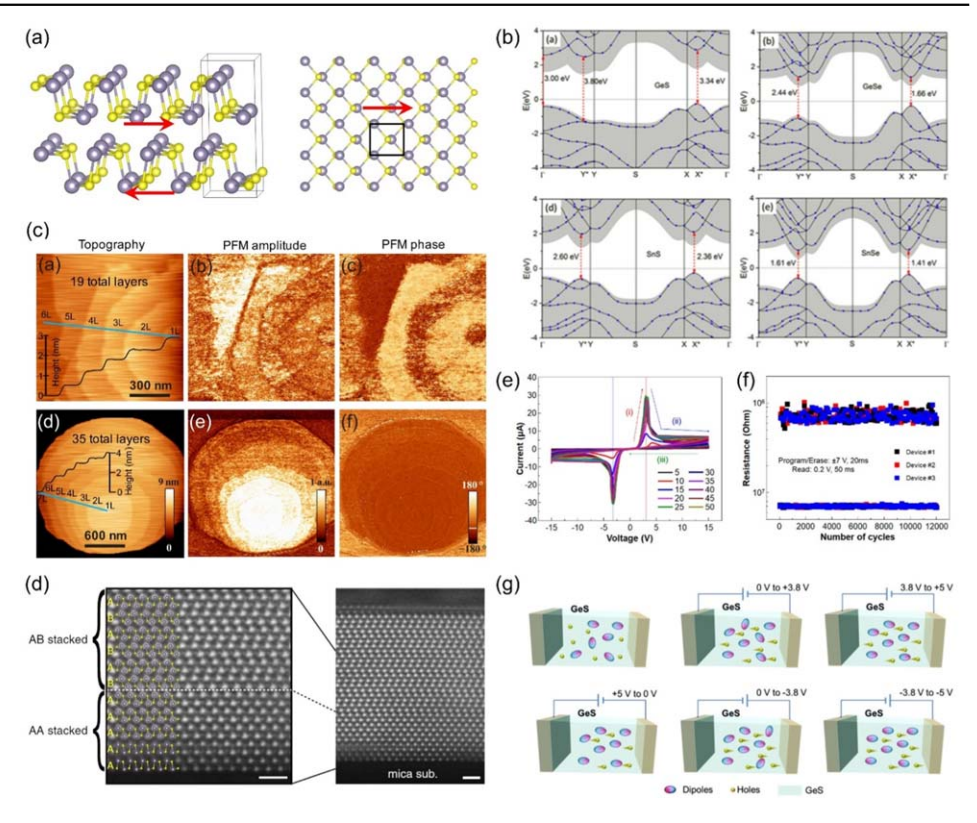


Figure 2. Group IV monochalcogenides (MXs). (a) Crystal structure of MX viewed from side (left) and top (right). Yellow and grey spheres correspond with chalcogen and metal atoms, respectively. Unit cells are represented with black solid lines. (b) Calculated band structures of monolayer GeS, GeSe, SnS, and SnSe. Adapted from [50] with permission. (c) Topography, PFM amplitude, and PFM phase images of AB- (top) and AA-stacked SnS (bottom), respectively. Adapted from [55] with permission. (d) Cross-section TEM images of 16 L SnS. Adapted from [52] with permission. Scale bars: 1 nm. (e) I-V curves of SnS device. The number of cycles are represented with different colors. (f) Resistance changes against applied p (fatigue test) of SnS thin film. Program/erase pulse voltage is ± 7 V and read voltage is 0.2 V. (e) and (f) were adapted from [53] with permission. (g) Schematic diagram demonstrating resistance change mechanism in GeS ferroelectric channel device. Adapted from [56] with permission.

where a stacking order change was observed for 16 L SnS (figure 2(d)) [52]. Based on the in-plane ferroelectricity, the MX devices displayed hysteresis in their *I–V* curves (figure 2(e)), indicating their potential for application as resistance switching memory (figure 2(f)) [53]. When a small forward bias is applied to an MX device, residual negatively polarized domains cause the device to exhibit a low-resistance state. As the forward bias exceeds the coercive force of MX, the polarizations of the domains switch in the positive direction, hindering the transport of charge carriers. When a higher voltage is applied, the current in the MX device is saturated and quenched by charge accumulation at the interface between SnS and the electrodes, leading to a high-resistance state (figure 2(g)) [51, 52, 56]. In addition, a synaptic device utilizing MX has been demonstrated by flipping and reversing the polarization of MXs domains through electrical spikes [53].

In addition to in-plane ferroelectricity, MXs have been reported to exhibit various other characteristics, including piezoelectric [57], bulk photovoltaic [56, 58], anisotropic thermoelectric [59, 60], and valley-dependent properties [61, 62]. However, owing to the strong interlayer interaction by the lone pair electrons in metal atoms [63, 64], the isolation of high-quality monolayer MXs and their characterisation have seldom been reported [52, 54]. Therefore, it is crucial to synthesize high-quality large-area monolayer MXs to bridge the gap between the theoretical understanding and practical applications of MXs.

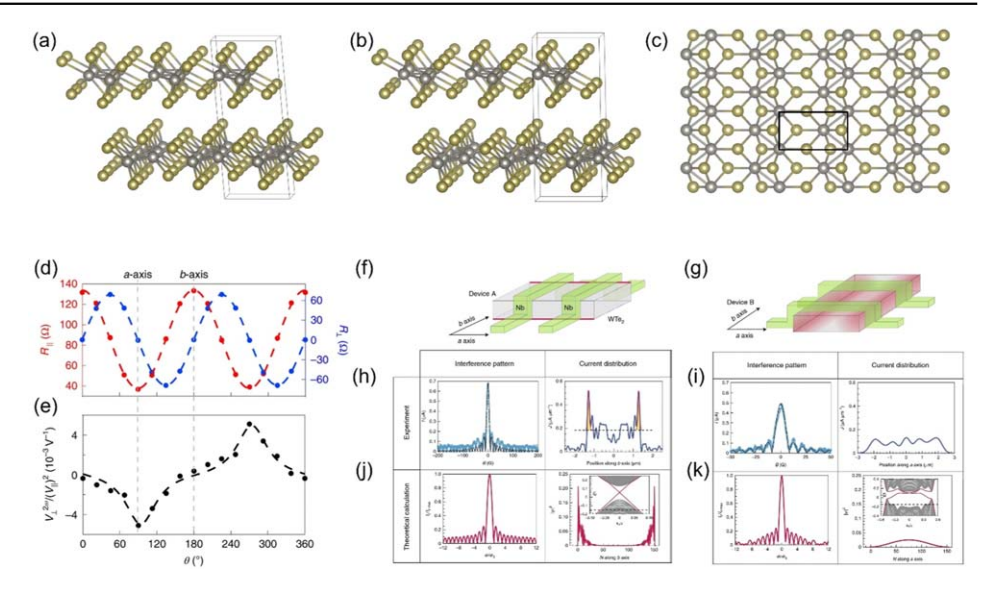


Figure 3. Group VI transition metal ditellurides. (a), (b) Crystal structure of 1T and T_d phase transition metal ditellurides viewed from side. Unit cells is represented with black cuboid. (c) Top view of monolayer 1T and T_d phase transition metal ditellurides. Unit cells is represented with black solid lines. (d) Longitudinal and transverse resistance of a WTe₂ device as a function of angle between b-axis and current bias. (e) Angle-dependent nonlinear Hall effect in WTe₂ device. (d) and (e) were adapted from [76] with permission. (f), (g) Schematic diagrams of WTe₂ Josephson junctions well-localized hinge states along the a-axis (f) and delocalized states along the b axis (g). (h), (i) Measured magnetic field interference patterns (left) and extracted spatial distributions of the Josephson current (right) of device A and B, respectively. (j), (k) Left: Theoretically calculated interference patterns of the critical current along the a-axis (h) and b-axis (i). Right: Theoretically calculated wave functions for the hinge states along the a-axis (j) and b-axis (k). Inset: the energy spectra of multilayer WTe₂ along the a axis (j) and b axis (k). (f)–(k) were adapted from [77] with permission.

2.3. Group VI transition metal ditellurides: phase transition and topological states

Group VI TMDCs (MX_2 , M = Mo, W; X = S, Se, Te) can exist in several polymorphs, depending on the coordination between the metal and chalcogen atoms. MoTe₂, similar to MoS₂ and MoSe₂, has a thermodynamically stable 2H-phase with a P6₃/mmc space group, in which the metal atoms are surrounded by six prismatically arranged tellurium atoms. 2H-MoTe₂ exhibits in-plane isotropy with semiconducting properties, while the metastable metallic 1T' phase of MoTe₂ shows in-plane anisotropic properties due to the dimerization of metal atoms along the *a*-axis caused by Peierls distortion (figure 3(a)) [65]. 1T'-MoTe₂ belongs to the monoclinic crystal system ($P2_1/m$ space group) with a *c*-axis inclined approximately 94° to the basal plane with inversion symmetry (figure 3(c)). The energy difference between the 2H and 1T' phases of MoTe₂ is only few tens of meV [65, 66], leading to extensive research on the phase transitions between these two phases using methods such as laser irradiation [67], thermal annealing [68], strain [69], electrical fields [70], and electrostatic doping [71].

The T_d phase is another metastable phase of MoTe₂ with a monolayer structure identical to that of the 1T' phase. However, the T_d phase has an orthorhombic structure (Pmn2₁ space group) with vertically stacked monolayers (figure 3(b)). In contrast to the 1T' phase, which has an inversion center between two adjacent layers, the T_d phase is noncentrosymmetric. The T_d -MoTe₂ can be obtained by cooling 1T'-MoTe₂ under 250 K [72, 73]. In contrast, for WTe₂, the T_d phase is stable under ambient conditions. The most intriguing feature of T_d -MoTe₂ and T_d -WTe₂ is their topological states, where the distortion in the metal atoms leads to the inversion of the valence and conduction bands [74, 75]. The inverted bands are further hybridized by spin—orbit coupling, which makes T_d -MoTe₂ and T_d -WTe₂ topologically nontrivial phases. Athough both

1T'-MoTe₂ and 1T'-WTe₂ are composed of identical monolayers with lattice distortion, they do not have topological characteristics due to the presence of inversion symmetry. Recently, in-plane anisotropy of the topological characteristics in T_d -WTe₂ has been further investigated. Kang *et al* reported the nonlinear anomalous Hall effect (AHE) under zero magnetic field [76]. The Hall voltage reached its maximum (minimum) when the bias current was parallel (perpendicular) to the W chain direction (figures 3(d) and (e)). Choi *et al* spatially resolved helical one-dimensional (1D) hinge structures in T_d -WTe₂ [77]. They found that the hinge states were localized only along the edges parallel to the direction of the W chain (*a*-axis) (figures 3(f)–(k)).

2.4. Rhenium dichalcogenides: multidomain structure with ferroelasticity

In contrast to the dimerization of metal atoms in 1T' or T_d phase MoTe₂ and WTe₂, ReX₂ (ReX₂, X = S, Se) exhibits in-plane anisotropy due to the clustering of four Re atoms. The presence of additional valence electrons in ReX2 leads to the formation of covalent bonds between Re atoms, resulting in the clustering of Re₄ units arranged in a rhombus shape (Re₄ rhombus) (figure 4(a)) [78–84]. The Re4 rhombuses are further connected by Re-Re bridges, forming unidirectional Re chains. The formation of Re₄ clusters induces lattice distortion, causing ReX₂ to belong to a triclinic crystal system with P1 space group. The substantially reduced symmetry of ReX₂ allows the directions of the lattice vectors to be arbitrarily defined. However, in this study, a-axis is defined as parallel to the short diagonal of the Re₄ rhombus, whereas b-axis is defined as the direction parallel to the Re chains, approximately 120° from the a-axis. There are conflicting statements about the electronic structure of ReS₂ whether it is indirect band gap or direct bandgap semiconductor. According to Tongay et al [85], the presence of the Re₄ cluster inhibits ordered stacking in ReS₂ and dramatically reduces the interlayer coupling with adjacent layers. Consequently, the weak interlayer coupling in ReS₂ preserve the material's direct bandgap characteristic from monolayer to bulk [85, 86]. However, other groups reported contradictory results demonstrating indirect to direct band transition from bulk to monolayer ReS₂ [87–89]. Zhou et al suggested that the conflicting observations regarding the band structure of few-layered ReS₂ stem from the stacking order of ReS2 bilayers, which induces change of interlayer interaction and consequent change of band nature [90].

Owing to its highly reduced symmetry, ReX₂ has six switchable domains. Two-fold rotation along the in-plane axis is not a symmetrical operation for ReX₂ [83]. As a result, there are two different types of domains in ReX₂ with parallel b-axes but opposite out-of-plane orientations (c-axes). These domains are denoted as 'c-up' (top images figures 4(b)-(d)) and '\overline{c}-up' (bottom images figures 4(b)-(d)) depending on the direction of the c-axis [80–84]. Additionally, the c-up and c-up domains can possess three different types of domains, respectively, which are related with approximately 60°-rotation [80–82] (figures 4(b)–(d)). These domains can coexist in a single flake of ReS2, and can be distinguished using polarized optical microscopy (POM) (figure 4(e)), polarized Raman spectroscopy (figure 4(f)), and TEM (figure 4(g)) [83, 84]. These six domains can be switched by reconstructing Re chains under electron-beam radiation [79], fracture propagation [91], and uniaxial strain [80]. Jeong et al observed an abrupt generation of new domains under uniaxial tensile strain (figure 4(h)) [80]. The newly generated domains are not perfectly restored even after strain relaxation, and the Raman shift exhibits hysteresis under strain (figure 4(i), (j)). These results demonstrate the ferroelasticity of ReS2. The ferroelasticity in ReX2 arises from the reconstruction of Re-Re bridges. This reconstruction, in turn, leads to a switching of the domain orientation, where the former and latter domains are related to a 120° rotation, followed by mirror reflection (figure 4(k)).

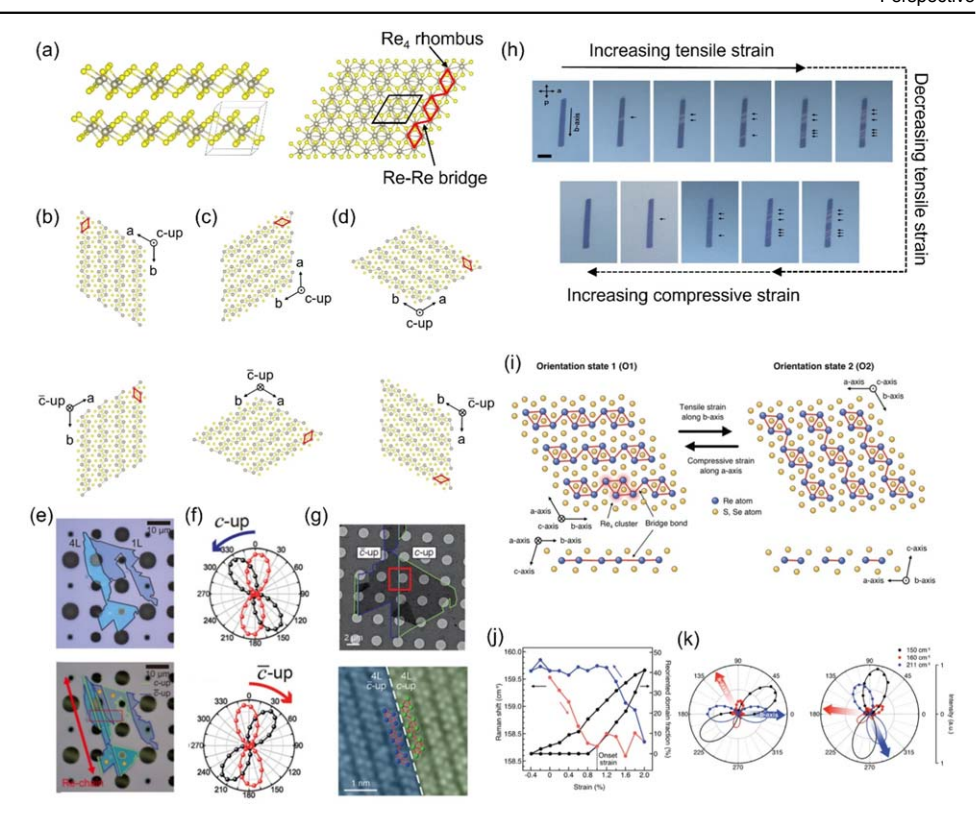


Figure 4. Rhenium dichalcogenides. (a) Crystal structure of ReX₂ viewed from side (left) and top (right). Yellow and grey spheres correspond with chalcogen and rhenium atoms, respectively. Unit cells are represented with black solid lines. Clustering of Re atoms is highlighted with red color. (b)–(d) Six different domains of ReX₂. Top (bottom) images in (b)–(d) are c-up (\bar{c} -up) domains. (e) Optical (top) and POM (bottom) images of ReS₂ flakes with c-up and \bar{c} -up domains. The incident polarization of POM is at ~45° with respect to the analyzer. (f) Polar plots of Raman intensities from c-up (top) and \bar{c} -up (bottom) domains. Red and black plots correspond with Raman mode 3 and 5, respectively. (g) TEM images of 4L-ReS₂ with c-up and \bar{c} -up domains. (e)–(g) were adapted from [84] with permission. (h) POM images of the evolution of the domain ReS₂ under uniaxial strain along the *b*-axis. The polarizer and analyzer are set perpendicular to each other. The reoriented domains are indicated with black arrows. Scale bar: 10 μ m. (i) Schematic diagram of ferroelastic domain switching of ReS₂ under uniaxial strain. (j) Change of Raman peak position (red and blue) and fraction of the switched domain width (black) of ReS₂ as a function of strain. (k) Polar plots of Raman peak intensities of intrinsic (left) and re-oriented ReS₂ domains (right), respectively. (h)–(k) were adapted from [80] with permission.

Multidomain structures have been observed in other in-plane anisotropic 2D materials synthesized by chemical vapor deposition (CVD) [92, 93]. Furthermore, the occurrence of ferroelasticity with domain switching has also been anticipated in other in-plane anisotropic 2D material [94, 95]. Nevertheless, to date, multidomain structures in exfoliated samples [84, 96] and the experimental implementation of domain switching have only been confirmed for ReX_2 [79, 80, 91]. These results may originate from the considerably low energy barrier height between the ReX_2 domains compared to other in-plane anisotropic 2D materials [79].

2.5. Other in-plane anisotropic 2D materials

In this section, we also introduce several in-plane anisotropic 2D materials.

Pnictogen atoms such as arsenic (As), antimony (Sb), and bismuth (Bi) can manifest as 2D allotropes. In α -phase 2D pnictogens, similar to MXs, four atoms are located at four different *z*-coordinates [97–102].

 α -MoO₃ is a layered transition metal oxide with an orthorhombic structure. The unit cell of α -MoO₃ is composed of two distorted octahedral double layers

loosely bonded together by weak vdW forces along the *b*-axis [103]. Within each individual layer, the octahedra are connected through corner sharing along the *a*-axis and edge sharing along the *c*-axis. Recently, α -MoO₃ has attracted significant interest because of its in-plane hyperbolic phonon-polaritions [104–106].

Group IVB transition metal trichalcogenides (MX₃, M = Ti, Zr, or Hf, X = S or Se) have a monoclinic crystal system in which the monolayer consists of a double layer of triangular 1D MX₃ units. Because the breakage of the interaction between the 1D chains and 2D layer requires similar energies, the MX₃ tend to be exfoliated into a whisker shape [107]. For TiS₃, its monolayer is expected to have direct bandgap with \sim 1.0 eV [108].

3. Twistronics in in-plane anisotropic 2D materials

The most popular topics in 2D materials and vdW heterostructures are moiré superlattices and twistronics [12–14]. When multiple layers of 2D materials are stacked with lattice mismatches or twist angles, they give rise to long-range quasiperiodic patterns known as moiré superlattices. As discussed in the Introduction, moiré superlattices exhibit unique physical properties that are not found in the original parent materials [15–23]. In addition to studies based on 2D materials with hexagonal symmetry, moiré superlattices based on in-plane anisotropic 2D materials have been consistently reported. These systems can induce more diverse phenomena owing to their additional degrees of freedom resulting from their reduced symmetry.

In this section, we introduce the theoretical and experimental results for vdW homobilayers with in-plane anisotropic 2D materials (BP/BP, MX/MX, or WTe₂/WTe₂) and vdW heterostructures with at least one parent material exhibiting in-plane anisotropy (graphene/BP or BP/WSe₂).

3.1. Twistronics in homobilayers with in-plane anisotropic 2D materials

Mathematically, the moiré superlattices of vdW homobilayers exhibit similar symmetry with that of their parent materials [12, 109]. For example, moiré superlattices formed between homogeneous in-plane anisotropic 2D materials with rectangular monolayers, such as BP, MXs, and MTe₂, exhibit long-range rectangular patterns. In other words, vdW homobilayers with in-plane anisotropic 2D materials exhibit moiré patterns with different periodicities along their in-plane orientations.

Kang et al theoretically investigated twisted bilayer BP (tbBP) with a twist angle smaller than 5.4° [110]. There are four kinds of high-symmetry local stacking configurations in tbBPs, named as AA, AB, AA', and AB'. AB stacking is the natural stacking order of bilayer BP, whereas AA, AA', and AB' can be obtained when the upper layer in the AB stacking is translated along (0,+y/2), (+x/2,0), and (+x/2,+y/2), respectively (figure 5(a)). Interestingly, the CBM and VBM of the tbBPs showed flat bands along the Γ -X (armchair) direction (figure 5(b)). The conduction band of tbBP shows a flat band regardless of the direction, resulting from the strong localization of the conduction wavefunction in all directions (localized on AB' stacking), whereas the valence wavefunction is localized along the x-direction (on AA and AB stacking). The flat bands indicate an extremely high effective mass, which in turn causes a sharp decrease in carrier mobility along the x-direction. Moreover, the carrier mobility along the y-direction can be further influenced by the twist angle. In particular at $\theta = 2.7^{\circ}$, the conduction wave function is highly localized even in the y-direction, which induces drastic reduction of electron mobility along the y-direction (figure 5(c)).

Moiré superlattices in twisted bilayer MXs (tbMXs) have recently been further examined. Keness *et al* and Zhang *et al* investigated electronic band structure of

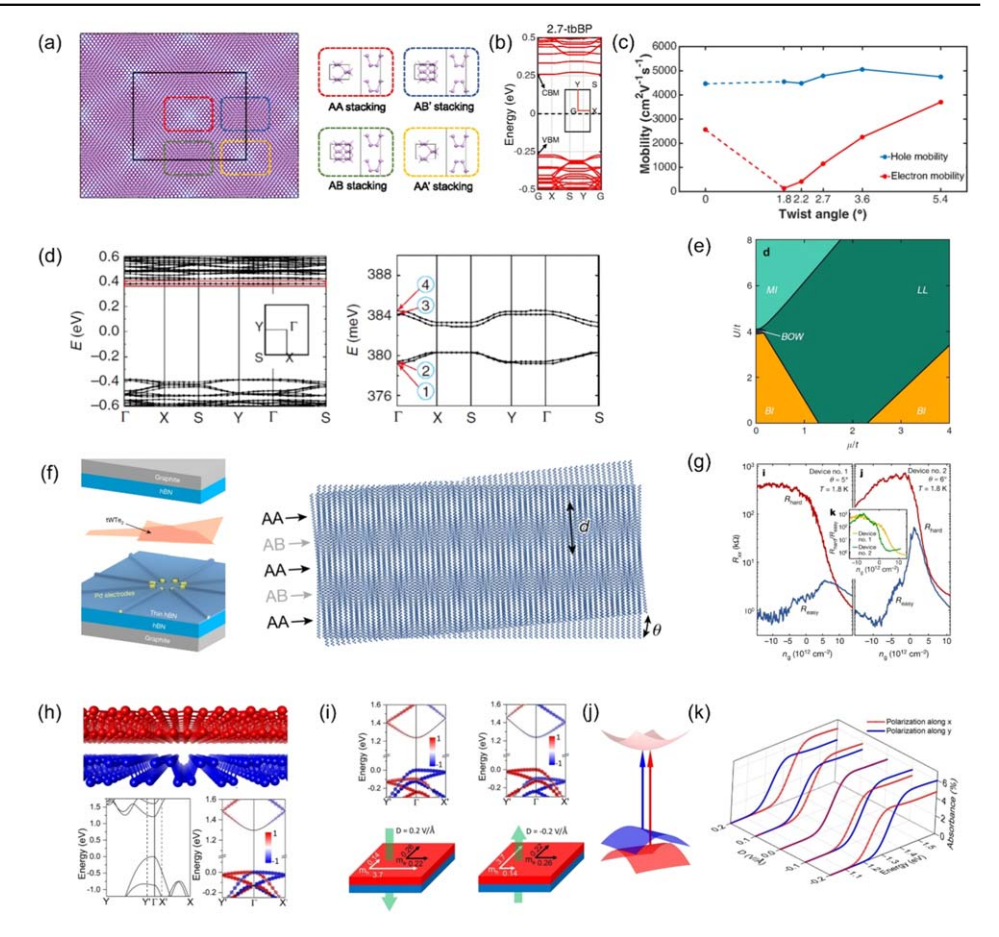


Figure 5. Twistronics in homobilayers with in-plane anisotropic 2D materials. (a) Moiré pattern formed on the tbBP with $\theta = 2.7^{\circ}$. The high-symmetry local stacking configurations and the supercell are represented with colored and black rectangles, respectively. The stacking configurations are shown in the right panels. (b) Calculated band structure of 2.7°-tbBP. (c) Deformation limited carrier mobility as a function of twist angle along the armchair direction. (a)-(c) were adapted from [110] with permission. (d) Calculated band structure of tbGeSe obtained from density functional theory using the local density approximation (LDA). Right images is a magnified image of red-boxed in the left image. (e) Phase diagram of tbGeSe depending on chemical potential μ , on-site repulsion U, and nearest-neighbor hopping t. (d)–(e) were adapted from [111] with permission. (f) Schematic diagrams of tbWTe2 device (left) and moiré patterns with only W atoms (right). (g) Gate-dependent four-probe resistances of two tbWTe2 devices with different twist angles. (f)-(g) were adapted from [113] with permission. (h) Schematic diagrams of 90°-tbBP (top), band structures of naturally stacked bilayer BP (bottom left) and 90°-tbBP (bottom right). (i) Band structures (top) and schematic diagrams of effective mass changes (bottom) in of 90°-tbBP under out-of-plane electric field. (j) Schematic diagram of optical transitions from VB of bottom BP (blue) and VB of top BP (red) to CB. (k) Optical absorption spectra of 90°-tbBP depending on gate bias and polarization. (h)–(k) were adapted from [114] with permission.

twisted bilayer GeSe (tbGeSe) and SnS (tbSnS), respectively [111, 112]. Because of reduced symmetry of MXs compared with BP, stacking configurations of tbMXs at twist angle θ and 180°- θ are not identical. As a result, there are eight distinct types of high-symmetry local stacking configurations in twisted bilayer MXs. Nevertheless, both tbGeSe and tbSnS exhibited charge carrier localization in 1D wires as well as 1D flat bands, similar to tbBP (figure 5(d)). Keness *et al* explained the dispersion and charge modulation along a 1D wire using the ionic Hubbard model [112]. They expected that, as a function of the twist angle and chemical potential, tbGeSe can show diverse phases of matter, such as band insulator (BI), Mott insulator (MI), bond oriented wave (BOW), and Luttinger liquid (LL) (figure 5(e)).

This expectation was recently fulfilled in a study on twisted bilayer 1 T'-WTe₂ (tbWTe₂) by Wang *et al* [113]. They fabricated 5°-tbWTe₂ by the tear and stack

method with ~ 7 nm spacing of moiré patterns between W atoms (figure 5(f)). In the hole-doped region, the two orthogonal directions exhibit a conductivity anisotropy ratio of ~ 1000 at 1.8 K (figure 5(g)). They also investigated the conductance power laws in both directions and interpreted their findings as indicative of the emergence of a two-dimensional anisotropic non-Fermi liquid phase with similarities to an LL.

VdW homobilayers with large twist angles have also been studied. Cao *et al* calculated the band structure of a BP homobilayer with a twist angle of 90° (figure 5(h)) [114]. Unlike naturally stacked bilayers, which show highly anisotropic band dispersion along the Γ -X (armchair) and Γ -Y (zigzag) direction (bottom left of figure 5(h)), band structure of the 90° -tbBP homobilayer is nearly isotropic around the Γ point. However, the VBM is separated into two sets of bands localized in the top (red) and bottom layers (blue) owing to weak interlayer hybridization (bottom right of figure 5(h)). The energy of each band can be shifted by an out-of-plane electric field, resulting in a gate-switchable effective mass anisotropy. The downward (upward) electric field increases the energy of the valence band attributed to the bottom (top) layer, thus hole effective mass of the vdW homostructure exhibits higher value along zigzag direction of bottom (top) BP layer (figure 5(i)). They also expected gate-tunable optical dichroism in 90° -tbBP (figures 5(j) and (k)).

As discussed above, vdW homobilayer composed with in-plane anisotropic 2D materials exhibit peculiar phenomena and strong anisotropy which cannot be obtained in vdW homobilayer with isotropic 2D materials. For small twisted angle, these system can be promising platforms to study strongly correlated 1D physics and to interpolate between 1D and 2D system. In contrast, a large-twisted-angle system can be utilized as an optoelectronic device with a higher degree of freedom, which can be modulated by an electrical field or optical polarization.

3.2. Twistronics in van der Waals heterostructures with in-plane anisotropic 2D materials

In addition to twisted homobilayers, several studies have focused on vdW heterostructures, which involve at least one parent material with in-plane anisotropy. Although extensive research has been conducted on vdW heterostructures involving in-plane anisotropic 2D materials, our attention has been focused on investigations that specifically explore the impact of moiré patterns on the modulation of orientation-dependent properties in such vdW heterostructures.

In these systems, the moiré patterns generally exhibit a parallelogram shape. Liu *et al* reported a sample-wide pseudomagnetic field (PMF) in a graphene/BP heterostructure [115]. They fabricated graphene/BP heterostructures by transferring monolayer graphene onto a few-layer BP. For the twist angle around $\theta=0^\circ$, the moiré patterns exhibit a pseudo 1D striped pattern with highly different periodicity ($\lambda_1=8$ nm and $\lambda_2=0.8$ nm at $\theta=1.03^\circ$) (figure 6(a)). The wavelengths and angles between them can be tuned by varying the twist angle, which, in turn, can modulate the strain texture in the heterostructure (figure 6(b)). The non-uniform strain patterns results in a shift of two different Dirac cones in opposite directions, inducing a PMF in the graphene/BP heterostructure (figure 6(c)). The angle-dependent moiré patterns in the graphene/BP heterostructure suggested that the magnitude and distribution of the PMF can be engineered by changing the twist angle between the 2D materials (figure 6(d)).

Akamatsu *et al* stacked multilayer BP on a monolayer WSe₂ and investigated the spontaneous photovoltaic effect (SPE) in the heterostructure [116]. When the armchair edges of BP and WSe₂ were aligned, the symmetries of WSe₂, the three mirror planes, and one three-fold rotational symmetry were reduced to one mirror plane parallel to the armchair edge of BP. In this reduced symmetry, electronic polarization appears along the mirror plane (figure 6(e)). Similar to the aforementioned graphene/BP heterostructures, the BP/WSe₂ interface exhibits strip-

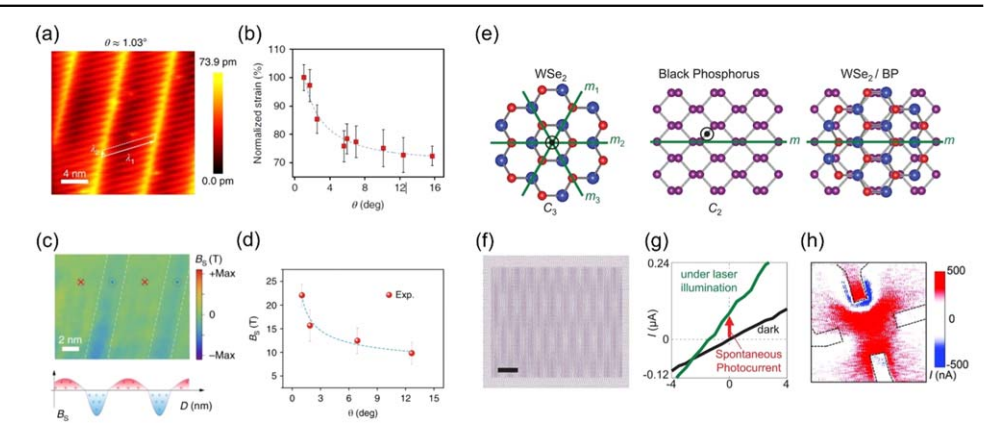


Figure 6. Twistronics in van der Waals heterostructures with in-plane anisotropic 2D materials (a) scanning tunneling microscopy image of graphene/BP heterostructure. (b) Calculated biaxial strain as a function of twist angle. (c) PMF texture in graphene/BP with 1.03°-twist angle. (d) Measured PMF as a function of twist angle. (a)–(d) were adapted from the [115] with permission. (e) Schematic illustrations of monolayer WSe₂ (left), BP (middle), and BP/WSe₂ heterostructure (right) with symmetry operations. (f) Moiré patterns of BP/WSe₂ heterostructure. The scale bar is 5 nm. (g) *I–V* characteristics of the BP/WSe₂ device under dark and laser illumination. (h) Photocurrent mapping of BP/WSe₂ device. (e)–(h) were adapted from the [116] with permission.

shaped moiré patterns (figure 6(f)). In the BP/WSe₂ device, a spontaneous photocurrent is observed under laser illumination (figure 6(g)). In contrast to the devices with only WSe₂ or BP, where the photocurrent is observed primarily around the electrodes, the BP/WSe₂ device exhibits the SPE even at locations far from the electrodes (figure 6(h)). Based on measurements of the photocurrent, depending on the excitation power and linear polarization angle of the laser, the authors attributed the SPE to the shift current, which is a result of the asymmetric shift of photoexcited electrons and holes in a non-centrosymmetric crystal [117, 118].

As demonstrated above, the presence of pseudo-1D moiré patterns in in-plane anisotropic 2D material-based vdW heterostructures enables the observation of novel phenomena that are not typically observed in moiré patterns between hexagonal 2D-materials. Moreover, it provides a means for manipulating the symmetry of two-dimensional materials, allowing isotropic materials to exhibit anisotropic phenomena. Therefore, this approach is expected to expand the field of 2D materials and vdW heterostructures significantly.

4. Challenges and perspective

In this perspective paper, we have introduced representative in-plane anisotropic 2D materials and twistronics based on them. However, several challenges need to be addressed in these fields: (1) even though exotic properties are expected for monolayer in-plane anisotropic 2D materials, their experimental implementation has been limited by the difficulty in fabricating monolayers caused by strong interlayer interactions. As a result, these materials exhibit insufficient control over quality, size, and thickness; (2) since many in-plane anisotropic 2D materials are prone to degradation under ambient conditions, research on passivation methods is necessary; (3) the electrical anisotropy ratio of most in-plane anisotropic 2D materials is relatively low, typically less than 10 orders of magnitude, and difficult to control. New approaches are required to increase the electrical anisotropy ratio and tunability, as demonstrated in [113] or [114]. (4) Although recent research has explored twistronics using in-plane anisotropic 2D materials, it still lags behind studies conducted with in-plane isotropic materials. Twistronics employing in-

plane anisotropic 2D materials offers the potential to unlock additional properties owing to their higher degrees of freedom. Therefore, it is crucial to undertake additional rigorous theoretical and experimental investigations encompassing a wide range of combinations to advance our understanding in this field. Addressing these challenges could significantly contribute to the advancement of the field of in-plane anisotropic 2D materials and their twistronics, as well as their application in orientation-dependent optoelectronic devices.

Acknowledgments

This work is supported by the National Research Foundation (NRF) of Korea funded by the Ministry of Science, ICT & Future Planning (2021R1A2C3014316, 2018M3D1A1058793, 2021H1D3A2A01045033) and Creative-Pioneering Researchers Program through Seoul National University (SNU). GHL acknowledges the support from the Research Institute of Advanced Materials (RIAM), Institute of Engineering Research (IER), Institute of Applied Physics (IAP), and inter-university semiconductor Research Center (ISRC) at the Seoul National University. YJ acknowledges the financial support from the US National Science Foundation (CAREER: 2142310).

Data availability statement

No new data were created or analysed in this study.

ORCID iDs

Yeonwoong Jung https://orcid.org/0000-0001-6042-5551 Gwan-Hyoung Lee https://orcid.org/0000-0002-3028-867X

References

- [1] Novoselov K S, Geim A K, Morozov S V, Jiang D, Zhang Y, Dubonos S V, Grigorieva I V and Firsov A A 2004 Electric field effect in atomically thin carbon films Science 306 666
- [2] Zhang Y, Tan Y W, Stormer H L and Kim P 2005 Experimental observation of the quantum Hall effect and Berry's phase in graphene *Nature* 438 201
- [3] Novoselov K S, Jiang Z, Zhang Y, Morozov S V, Stormer H L, Zeitler U, Maan J C, Boebinger G S, Kim P and Geim A K 2007 Room-temperature quantum Hall effect in graphene *Science* 315 1379
- [4] Bolotin K I, Ghahari F, Shulman M D, Stormer H L and Kim P 2009 Observation of the fractional quantum Hall effect in graphene Nature 462 196
- [5] Mak K F, He K, Lee C, Lee G H, Hone J, Heinz T F and Shan J 2013 Tightly bound trions in monolayer MoS₂ Nat. Mater. 12 207
- [6] Cheiwchanchamnangij T and Lambrecht W R L 2012 Quasiparticle band structure calculation of monolayer, bilayer, and bulk MoS₂ Phys. Rev.B 85 205302
- [7] Watanabe K, Taniguchi T and Kanda H 2004 Direct-bandgap properties and evidence for ultraviolet lasing of hexagonal boron nitride single crystal *Nat. Mater.* **3** 404
- [8] Lee G-H, Yu Y-J, Lee C, Dean C, Shepard K L, Kim P and Hone J 2011 Electron tunneling through atomically flat and ultrathin hexagonal boron nitride *Appl. Phys. Lett.* **99** 243114
- [9] Geim A K and Grigorieva I V 2013 Van der Waals heterostructures Nature 499 419
- [10] Novoselov K S, Mishchenko A, Carvalho A and Castro Neto A H 2016 2D materials and van der Waals heterostructures Science 353 aac9439
- [11] Liu Y, Weiss N O, Duan X, Cheng H-C, Huang Y and Duan X 2016 Van der Waals heterostructures and devices Nat. Rev. Mater. 1 16042
- [12] Tang K and Qi W 2020 Moiré-pattern-tuned electronic structures of van der Waals heterostructures Adv. Func. Mater. 30 2002672

- [13] Andrei E Y, Efetov D K, Jarillo-Herrero P, MacDonald A H, Mak K F, Senthil T, Tutuc E, Yazdani A and Young A F 2021 The marvels of moiré materials *Nat. Rev. Mater.* 6 201
- [14] He F, Zhou Y, Ye Z, Cho S H, Jeong J, Meng X and Wang Y 2021 Moiré patterns in 2D Materials: a review ACS Nano 15 5944
- [15] Cao Y, Fatemi V, Fang S, Watanabe K, Taniguchi T, Kaxiras E and Jarillo-Herrero P 2018 Unconventional superconductivity in magic-angle graphene superlattices *Nature* 556 43
- [16] Cao Y et al 2018 Correlated insulator behaviour at half-filling in magic-angle graphene superlattices Nature 556 80
- [17] Yasuda K, Wang X, Watanabe K, Taniguchi T and Jarillo-Herrero P 2021 Stackingengineered ferroelectricity in bilayer boron nitride Science 372 1458
- [18] Vizner Stern M, Waschitz Y, Cao W, Nevo I, Watanabe K, Taniguchi T, Sela E, Urbakh M, Hod O and Ben Shalom M 2021 Interfacial ferroelectricity by van der Waals sliding *Science* 372 1462
- [19] Woods C R, Ares P, Nevison-Andrews H, Holwill M J, Fabregas R, Guinea F, Geim A K, Novoselov K S, Walet N R and Fumagalli L 2021 Charge-polarized interfacial superlattices in marginally twisted hexagonal boron nitride *Nat. Commun.* 12 347
- [20] Wang X, Yasuda K, Zhang Y, Liu S, Watanabe K, Taniguchi T, Hone J, Fu L and Jarillo-Herrero P 2022 Interfacial ferroelectricity in rhombohedral-stacked bilayer transition metal dichalcogenides *Nat. Nanotech.* 17 367
- [21] Seyler K L, Rivera P, Yu H, Wilson N P, Ray E L, Mandrus D G, Yan J, Yao W and Xu X 2019 Signatures of moire-trapped valley excitons in MoSe₂/WSe₂ heterobilayers *Nature* 567 66
- [22] Tran K et al 2019 Evidence for moiré excitons in van der Waals heterostructures Nature 567 71
- [23] Yuan L, Zheng B, Kunstmann J, Brumme T, Kuc A B, Ma C, Deng S, Blach D, Pan A and Huang L 2020 Twist-angle-dependent interlayer exciton diffusion in WS₂-WSe₂ heterobilayers *Nat. Mater.* 19 617
- [24] Wei Q and Peng X 2014 Superior mechanical flexibility of phosphorene and few-layer black phosphorus Appl. Phys. Lett. 104 251915
- [25] Jiang J-W and Park H S 2014 Mechanical properties of single-layer black phosphorus J. Phys. D 47 385304
- [26] Tao J et al 2015 Mechanical and electrical anisotropy of few-layer black phosphorus ACS Nano 9 11362
- [27] Vaquero-Garzon L, Frisenda R and Castellanos-Gomez A 2019 Anisotropic buckling of few-layer black phosphorus Nanoscale 11 12080
- [28] Rudenko A N and Katsnelson M I 2014 Quasiparticle band structure and tight-binding model for single- and bilayer black phosphorus *Phys. Rev.* B 89 201408
- [29] Cai Y, Zhang G and Zhang Y-W 2014 Layer-dependent band alignment and work function of few-layer phosphorene Sci. Rep. 4 6677
- [30] Qiao J, Kong X, Hu Z X, Yang F and Ji W 2014 High-mobility transport anisotropy and linear dichroism in few-layer black phosphorus *Nat. Commun.* 5 4475
- [31] Li L et al 2017 Direct observation of the layer-dependent electronic structure in phosphorene Nat. Nanotech. 12 21
- [32] Yuan H et al 2015 Polarization-sensitive broadband photodetector using a black phosphorus vertical p-n junction Nat. Nanotech. 10 707
- [33] Wu J, Mao N, Xie L, Xu H and Zhang J 2015 Identifying the crystalline orientation of black phosphorus using angle-resolved polarized Raman spectroscopy *Angew. Chem. Int. Ed.* 54 2366
- [34] Xia F, Wang H and Jia Y 2014 Rediscovering black phosphorus as an anisotropic layered material for optoelectronics and electronics Nat. Commun. 5 4458
- [35] Snure M, Vangala S and Walker D 2016 Probing phonon and electrical anisotropy in black phosphorus for device alignment Opt. Mater. Express 6 1751
- [36] Liu Y, Low T and Ruden P P 2016 Mobility anisotropy in monolayer black phosphorus due to scattering by charged impurities *Phys. Rev. B* 93 165402
- [37] Low T, Rodin A S, Carvalho A, Jiang Y, Wang H, Xia F and Castro Neto A H 2014 Tunable optical properties of multilayer black phosphorus thin films *Phys. Rev. B* 90 075434
- [38] Wang X, Jones A M, Seyler K L, Tran V, Jia Y, Zhao H, Wang H, Yang L, Xu X and Xia F 2015 Highly anisotropic and robust excitons in monolayer black phosphorus *Nat. Nanotech.* 10 517
- [39] Mao N *et al* 2016 Optical anisotropy of black phosphorus in the visible regime *J. Am. Chem. Soc.* **138** 300
- [40] Xin W, Jiang H B, Sun T Q, Gao X G, Chen S N, Zhao B, Yang J J, Liu Z B, Tian J G and Guo C L 2019 Optical anisotropy of black phosphorus by total internal reflection *Nano Mater. Sci.* 1 304
- [41] Lee S *et al* 2015 Anisotropic in-plane thermal conductivity of black phosphorus nanoribbons at temperatures higher than 100 K *Nat. Commun.* **6** 8573
- [42] Sun B, Gu X, Zeng Q, Huang X, Yan Y, Liu Z, Yang R and Koh Y K 2017 Temperature dependence of anisotropic thermal-conductivity tensor of bulk black phosphorus Adv. Mater. 29 1603297

- [43] Kim J, Lee J U, Lee J, Park H J, Lee Z, Lee C and Cheong H 2015 Anomalous polarization dependence of Raman scattering and crystallographic orientation of black phosphorus *Nanoscale* 7 18708
- [44] Ribeiro H B, Pimenta M A, de Matos C J, Moreira R L, Rodin A S, Zapata J D, de Souza E A and Castro Neto A H 2015 Unusual angular dependence of the Raman response in black phosphorus ACS Nano 9 4270
- [45] Zhong Q and Pang X 2023 Exploring the oxidation mechanisms of black phosphorus: a review J. Mater. Sci. 58 2068
- [46] Ziletti A, Carvalho A, Campbell D K, Coker D F and Castro Neto A H 2015 Oxygen defects in phosphorene *Phys. Rev. Lett.* 114 046801
- [47] Wood J D, Wells S A, Jariwala D, Chen K S, Cho E, Sangwan V K, Liu X, Lauhon L J, Marks T J and Hersam M C 2014 Effective passivation of exfoliated black phosphorus transistors against ambient degradation *Nano Lett.* 14 6964
- [48] Chen X et al 2015 High-quality sandwiched black phosphorus heterostructure and its quantum oscillations Nat. Commun. 6 7315
- [49] Dickerson W, Tayari V, Fakih I, Korinek A, Caporali M, Serrano-Ruiz M, Peruzzini M, Heun S, Botton G A and Szkopek T 2018 Phosphorus oxide gate dielectric for black phosphorus field effect transistors Appl. Phys. Lett. 112 173101
- [50] Xu L, Yang M, Wang S J and Feng Y P 2017 Electronic and optical properties of the monolayer group-IV monochalcogenides MX (M = Ge,Sn; X = S,Se,Te) Phys. Rev.B 95 235434
- [51] Bao Y et al 2019 Gate-tunable in-plane ferroelectricity in few-layer SnS Nano Lett. 19 5109
- [52] Higashitarumizu N, Kawamoto H, Lee C J, Lin B H, Chu F H, Yonemori I, Nishimura T, Wakabayashi K, Chang W H and Nagashio K 2020 Purely in-plane ferroelectricity in monolayer SnS at room temperature *Nat. Commun.* 11 2428
- [53] Kwon K C et al 2020 In-plane ferroelectric tin monosulfide and its application in a ferroelectric analog synaptic device ACS Nano 14 7628
- [54] Chang K, Kuster F, Miller B J, Ji J R, Zhang J L, Sessi P, Barraza-Lopez S and Parkin S S P 2020 Microscopic manipulation of ferroelectric domains in SnSe monolayers at room temperature *Nano Lett.* 20 6590
- [55] Sutter P, Komsa H P, Lu H, Gruverman A and Sutter E 2021 Few-layer tin sulfide (SnS): controlled synthesis, thickness dependent vibrational properties, and ferroelectricity *Nano Today* 37 101082
- [56] Yan Y, Deng Q, Li S, Guo T, Li X, Jiang Y, Song X, Huang W, Yang J and Xia C 2021 Inplane ferroelectricity in few-layered GeS and its van der Waals ferroelectric diodes *Nanoscale* 13 16122
- [57] Fei R, Li W, Li J and Yang L 2015 Giant piezoelectricity of monolayer group IV monochalcogenides: SnSe, SnS, GeSe, and GeS Appl. Phys. Lett. 107 173104
- [58] Rangel T, Fregoso B M, Mendoza B S, Morimoto T, Moore J E and Neaton J B 2017 Large bulk photovoltaic effect and spontaneous polarization of single-layer monochalcogenides *Phys. Rev. Lett.* 119 067402
- [59] Chang C et al 2018 3D charge and 2D phonon transports leading to high out-of-plane ZT in n-type SnSe crystals Science 360 778
- [60] Zhao L D, Lo S H, Zhang Y, Sun H, Tan G, Uher C, Wolverton C, Dravid V P and Kanatzidis M G 2014 Ultralow thermal conductivity and high thermoelectric figure of merit in SnSe crystals *Nature* 508 373
- [61] Hanakata P Z, Carvalho A, Campbell D K and Park H S 2016 Polarization and valley switching in monolayer group-IV monochalcogenides *Phys. Rev. B* 94 035304
- [62] Rodin A S, Gomes L C, Carvalho A and Castro Neto A H 2016 Valley physics in tin (II) sulfide *Phys. Rev. B* **93** 045431
- [63] Song H-Y and Lü J-T 2018 Density functional theory study of inter-layer coupling in bulk tin selenide Chem. Phys. Lett. 695 200
- [64] Lefebvre I, Szymanski M A, Olivier-Fourcade J and Jumas J C 1998 Electronic structure of tin monochalcogenides from SnO to SnTe Phys. Rev. B 58 1896
- [65] Keum D H et al 2015 Bandgap opening in few-layered monoclinic MoTe₂ Nat. Phys. 11 482
- [66] Duerloo K A, Li Y and Reed E J 2014 Structural phase transitions in two-dimensional Moand W-dichalcogenide monolayers Nat. Commun. 5 4214
- [67] Cho S et al 2015 Phase patterning for ohmic homojunction contact in MoTe₂ Science 349 625
- [68] Ryu H et al 2021 Anomalous dimensionality-driven phase transition of MoTe₂ in van der Waals heterostructure Adv. Func. Mater. 31 2107376
- [69] Song S, Keum D H, Cho S, Perello D, Kim Y and Lee Y H 2016 Room temperature semiconductor-metal transition of MoTe₂ thin films engineered by strain *Nano Lett.* **16** 188
- [70] Zhang F, Zhang H, Krylyuk S, Milligan C A, Zhu Y, Zemlyanov D Y, Bendersky L A, Burton B P, Davydov A V and Appenzeller J 2019 Electric-field induced structural transition in vertical MoTe₂ and Mo_{1-x}W_xTe₂-xbased resistive memories *Nat. Mater.* 18 55
- [71] Wang Y et al 2017 Structural phase transition in monolayer MoTe₂ driven by electrostatic doping Nature 550 487
- [72] Lv Y-Y et al 2017 The relationship between anisotropic magnetoresistance and topology of Fermi surface in T_d-MoTe₂ crystal J. Appl. Phys. 122 045102

- [73] Clarke R, Marseglia E and Hughes H P 1978 A low-temperature structural phase transition in β-MoTe₂ Philos. Mag. B 38 121
- [74] Qian X, Liu J, Fu L and Li J 2014 Quantum spin Hall effect in two-dimensional transition metal dichalcogenides Science 346 1344
- [75] Tang S et al 2017 Quantum spin Hall state in monolayer 1T'-WTe₂ Nat. Phys. 13 683
- [76] Kang K, Li T, Sohn E, Shan J and Mak K F 2019 Nonlinear anomalous Hall effect in few-layer WTe₂ Nat. Mater. 18 324
- [77] Choi Y B et al 2020 Evidence of higher-order topology in multilayer WTe₂ from Josephson coupling through anisotropic hinge states Nat. Mater. 19 974
- [78] Choi J H and Jhi S H 2018 Origin of distorted 1T-phase ReS₂: first-principles study J. Phys. Condens. 30 105403
- [79] Lin Y C, Komsa H P, Yeh C H, Bjorkman T, Liang Z Y, Ho C H, Huang Y S, Chiu P W, Krasheninnikov A V and Suenaga K 2015 Single-layer ReS₂: two-dimensional semiconductor with tunable in-plane anisotropy ACS Nano 9 11249
- [80] Jeong J et al 2022 Ferroelastic-ferroelectric multiferroicity in van der Waals rhenium dichalcogenides Adv. Mater. 34 2108777
- [81] Choi Y, Kim K, Lim S Y, Kim J, Park J M, Kim J H, Lee Z and Cheong H 2020 Complete determination of the crystallographic orientation of ReX₂ (X = S, Se) by polarized Raman spectroscopy *Nanoscale Horiz* 5 308
- [82] Li X, Wang X, Hong J, Liu D, Feng Q, Lei Z, Liu K, Ding F and Xu H 2019 Nanoassembly growth model for subdomain and grain boundary formation in 1T' layered ReS₂ Adv. Func. Mater. 29 1906385
- [83] Hart L, Dale S, Hoye S, Webb J L and Wolverson D 2016 Rhenium dichalcogenides: layered semiconductors with two vertical orientations *Nano Lett.* 16 1381
- [84] Park J M, Lee S, Na W, Kim K and Cheong H 2022 Precise determination of offset between optical axis and Re-chain direction in rhenium disulfide ACS Nano 16 9222
- [85] Tongay S et al 2014 Monolayer behaviour in bulk ReS₂ due to electronic and vibrational decoupling Nat. Commun. 5 3252
- [86] Jariwala B, Voiry D, Jindal A, Chalke B A, Bapat R, Thamizhavel A, Chhowalla M, Deshmukh M and Bhattacharya A 2016 Synthesis and characterization of ReS₂ and ReSe₂ layered chalcogenide single crystals *Chem. Mater.* 28 3352
- [87] Gehlmann M et al 2017 Direct observation of the band gap transition in atomically thin ReS₂ Nano Lett. 17 5187
- [88] Webb J L, Hart L S, Wolverson D, Chen C, Avila J and Asensio M C 2017 Electronic band structure of ReS₂ by high-resolution angle-resolved photoemission spectroscopy *Phys. Rev.* B 96 115205
- [89] Aslan B, Chenet D A, van der Zande A M, Hone J C and Heinz T F 2015 Linearly polarized excitons in single- and few-layer ReS₂ crystals ACS Photon. 3 96
- [90] Zhou Y et al 2020 Stacking-order-driven optical properties and carrier dynamics in ReS₂ Adv. Mater. 32 1908311
- [91] Huang L et al 2020 Anomalous fracture in two-dimensional rhenium disulfide Sci. Adv. 6 eabc2282
- [92] Zhu M et al 2019 Linear dichroism and nondestructive crystalline identification of anisotropic semimetal few-layer MoTe₂ Small 15 1903159
- [93] Hoang A T, Shinde S M, Katiyar A K, Dhakal K P, Chen X, Kim H, Lee S W, Lee Z and Ahn J H 2018 Orientation-dependent optical characterization of atomically thin transition metal ditellurides *Nanoscale* 10 21978
- [94] Li W and Li J 2016 Ferroelasticity and domain physics in two-dimensional transition metal dichalcogenide monolayers Nat. Commun. 7 10843
- [95] Wu M and Zeng X C 2016 Intrinsic ferroelasticity and/or multiferroicity in two-dimensional phosphorene and phosphorene analogues *Nano Lett.* 16 3236
- [96] Yu W et al 2020 Domain engineering in ReS₂ by coupling strain during electrochemical exfoliation Adv. Func. Mater. 30 2003057
- [97] Hogan C, Lechifflart P, Brozzesi S, Voronovich-Solonevich S, Melnikov A, Flammini R, Sanna S and Holtgrewe K 2021 Theoretical study of stability, epitaxial formation, and phase transformations of two-dimensional prictogen allotropes *Phys. Rev. B* 104 245421
- [98] Ares P, Palacios J J, Abellan G, Gomez-Herrero J and Zamora F 2018 Recent progress on antimonene: a new bidimensional material Adv. Mater. 30 1703771
- [99] Shi Z Q, Li H, Yuan Q Q, Xue C L, Xu Y J, Lv Y Y, Jia Z Y, Chen Y, Zhu W and Li S C 2020 Kinetics-limited two-step growth of van der Waals puckered honeycomb Sb monolayer ACS Nano 14 16755
- [100] Shi Z Q et al 2020 Tuning the electronic structure of an α -antimonene monolayer through interface engineering Nano Lett. **20** 8408
- [101] Gou J, Bai H, Zhang X, Huang Y L, Duan S, Ariando A, Yang S A, Chen L, Lu Y and Wee A T S 2023 Two-dimensional ferroelectricity in a single-element bismuth monolayer Nature 617 67
- [102] Li Y, Yuan Q, Guo D, Lou C, Cui X, Mei G, Petek H, Cao L, Ji W and Feng M 2023 1D electronic flat bands in untwisted moiré superlattices Adv. Mater. 35 2300572

- [103] Kim J H, Dash J K, Kwon J, Hyun C, Kim H, Ji E and Lee G-H 2018 Van der Waals epitaxial growth of single crystal α -MoO₃ layers on layered materials growth templates 2D Mater. 6 015016
- [104] Ma W et al 2018 In-plane anisotropic and ultra-low-loss polaritons in a natural van der Waals crystal Nature 562 557
- [105] Zheng Z et al 2019 A mid-infrared biaxial hyperbolic van der Waals crystal Sci. Adv. 5 eaav869
- [106] Zheng Z et al 2018 Highly confined and tunable hyperbolic phonon polaritons in van der Waals semiconducting transition metal oxides Adv. Mater. 30 1705318
- [107] Lipatov A et al 2018 Quasi-1D TiS₃ nanoribbons: mechanical exfoliation and thicknessdependent Raman spectroscopy ACS Nano 12 12713
- [108] Dai J and Zeng X C 2015 Titanium trisulfide monolayer: theoretical prediction of a new direct-gap semiconductor with high and anisotropic carrier mobility *Angew. Chem. Int. Ed.* 54 7572
- [109] Hermann K 2012 Periodic overlayers and moire patterns: theoretical studies of geometric properties J. Phys. Condens. 24 314210
- [110] Kang P, Zhang W-T, Michaud-Rioux V, Kong X-H, Hu C, Yu G-H and Guo H 2017 Moiré impurities in twisted bilayer black phosphorus: effects on the carrier mobility *Phys. Rev. B* 96 195406
- [111] Kennes D M, Xian L, Claassen M and Rubio A 2020 One-dimensional flat bands in twisted bilayer germanium selenide Nat. Commun. 11 1124
- [112] Zhang L, Zhang X and Lu G 2021 One-dimensional flat bands and anisotropic moiré excitons in twisted tin sulfide bilayers *Chem. Mater.* **33** 7432
- [113] Wang P et al 2022 One-dimensional Luttinger liquids in a two-dimensional moiré lattice Nature 605 57
- [114] Cao T, Li Z, Qiu D Y and Louie S G 2016 Gate switchable transport and optical anisotropy in 90 degrees twisted bilayer black phosphorus Nano Lett. 16 5542
- [115] Liu Y et al 2018 Tailoring sample-wide pseudo-magnetic fields on a graphene-black phosphorus heterostructure Nat. Nanotechnol. 13 828
- [116] Akamatsu T *et al* 2021 A van der Waals interface that creates in-plane polarization and a spontaneous photovoltaic effect *Science* 372 68
- [117] Cook A M, de Juan F B M F, Coh S and Moore J E 2017 Design principles for shift current photovoltaics *Nat. Commun.* **8** 14176
- [118] Tan L Z, Zheng F, Young S M, Wang F, Liu S and Rappe A M 2016 Shift current bulk photovoltaic effect in polar materials—hybrid and oxide perovskites and beyond NPJ Comput. Mater. 2 16026
- [119] Chen Z et al 2022 In-plane optical and electrical anisotropy in low-symmetry layered GeS microribbons NPG Asia Mater. 14 41
- [120] Zhou X, Hu X, Jin B, Yu J, Liu K, Li H and Zhai T 2018 Highly anisotropic GeSe nanosheets for phototransistors with ultrahigh photoresponsivity Adv. Sci. 5 1800478
- [121] Wolverson D, Crampin S, Kazemi A S, Ilie A and Bending S J 2014 Raman spectra of monolayer, few-layer, and bulk ReSe₂: an anisotropic layered semiconductor ACS Nano 8 11154